Computers and Structures 275 (2023) 106938

Contents lists available at ScienceDirect

Computers and Structures

journal homepage: www.elsevier.com/locate/compstruc

Mass matrices for elastic continua with micro-inertia

F. Gómez-Silva [a,*], H. Askes [b]

[a] Department of Continuum Mechanics and Structural Analysis, University Carlos III of Madrid, Avda. de la Universidad, 30, 28911 Leganés, Madrid, Spain
[b] Faculty of Engineering Technology, University of Twente, Drienerlolaan 5, 7522 NB Enschede, the Netherlands

ARTICLE INFO

Article history:
Received 19 July 2022
Accepted 1 November 2022
Available online 18 November 2022

Keywords:
Micro-inertia models
Length scale
Numerical analysis
High-order mass matrices
Natural frequencies

ABSTRACT

In this paper, the finite element discretization of non-classical continuum models with micro-inertia is analysed. The focus is on micro-inertia extensions of the one-dimensional rod model, the beam bending theories of Euler–Bernoulli and Rayleigh, and the two-dimensional membrane model. The performance of a variety of mass matrices is assessed by comparing the natural frequencies and their modes with those of the associated discrete systems, and it is demonstrated that the use of higher-order mass matrices reduces errors and improves convergence rates. Furthermore, finite element sizes *larger* than the corresponding physical length scale are shown to be sufficient to capture the natural frequencies, thus facilitating numerical models that are not only reliable but also computationally efficient.

1. Introduction

It is well known that matter presents internal microscopic structures that can affect its dynamic behaviour. The influence of these microstructural length scales on the macrostructural response is commonly denominated as *scale effect*. Scale effects may appear in nano- and micro-electromechanical systems [1], such as robotics [2] and biosensing [3], as well as in inhomogeneous materials, composites or metamaterials [4–7]. This latter type of materials has been used as lightweight structures, energy absorption systems or vibration control systems [8,9] due to improved static and dynamic performance of lattice-type materials compared to their solid counterparts. Thus, the exploration these materials is important and, by implication, the investigation of scale effects in these materials is relevant.

One particular manifestation of scale effects is dispersive wave propagation: perturbations with different wave lengths may propagate through the solid with different velocities, as has been pointed out in several experimental studies [10–13]. To simulate this behaviour, discrete models can be used that include each micro-structural element explicitly. However, such an approach requires a significant computational effort due to the a large number of degrees of freedom.

Concerning the alternative strategy of using continuum models, classical theories may fail in those involving high-frequency ranges, where the influence of scale effects becomes more relevant. For this reason, non-classical continuum models, capable of capturing the scale effects with a lower computational cost than discrete ones, have been pursued from the 1960s. Seminal works include those by Mindlin [14], Eringen [15,16] and Krumhansl [17,18], with more recent studies focussing on the implementation of generalized continuum theories to solve problems concerning beams [19,20], membranes [21] or plates [22], among others. In order to relate the additional material parameters to the mechanical and geometric properties of the underlying microstructure, continualization methods may be applied to discrete lattice systems. Extensive information about the application of continualization techniques to lattice systems can be found in the literature, for different models such as rods [23–26], beam theories considering bending [27–29] or bending with shear [30–33], membranes [34–37] or plates [38,39].

The non-classical continuum models discussed above are able to capture scale effects via the introduction of higher-order derivative terms in the governing equations (typically by additional space or space–time derivatives of the relevant state variables), which are accompanied by internal length scales (characteristic length of the lattice system). A detailed discussion on the ability to capture dispersive wave propagation through the addition of micro-inertia and strain gradient terms in the continuum governing equations can be found in [40]. Nonetheless, the inclusion of strain gradient terms leads to the need for extra boundary conditions, the physical meaning of which remains a subject of debate (but see the work of Froiio and coworkers [41,42] for an insightful interpretation). Moreover, strain gradient terms often require additional continuity of the interpolants [43].

* Corresponding author.
E-mail address: frgomezs@ing.uc3m.es (F. Gómez-Silva).

https://doi.org/10.1016/j.compstruc.2022.106938
0045-7949/

For these reasons, non-classical continuum models with micro-inertia only are pursued here. These models include additional spatial gradients of the accelerations, leading to so-called micro-inertia modifications of classical elasticity, and have been widely studied in recent years [44–48]. These works provide different microstructural derivations of the micro-inertia terms, revealing the common feature that the additional higher-order derivatives are accompanied by length scales related to the micro-structural geometry, such as the distance between particles in lattices or the size of the representative volume element in heterogeneous materials. The ability of these types of models to capture scale effects has been proven in several fields such as metamaterials [49], composite structures [50] and carbon nanotubes [51]. In addition, these approaches present certain advantages in numerical simulations, such as increasing the critical time step in conditionally stable time integration algorithms [52] and a straightforward implementation into existing finite element codes, since the continuity requirements on the interpolants are typically not affected by the inclusion of micro-inertia.

In this work, our aim is to develop effective and efficient finite element discretizations of continuum models with micro-inertia. Firstly, we propose the use of higher-order mass matrices, defined as linear combinations of the consistent mass matrix and the lumped mass matrix or of the consistent mass matrix and the stiffness matrix – to the best of the authors' knowledge, this has not been attempted for continuum models with micro-inertia. Secondly, we present formulations that allow the use of finite element sizes *larger* than the corresponding physical length-scale (equivalent to the characteristic length in a lattice system), thus reducing the computational costs that would be required to solve the associated discrete lattice system. To do this, we have studied a number of models here, namely the axial rod model, the bending theories of Euler–Bernoulli and Rayleigh, and the two-dimensional membrane model, anticipating that the insights gained from these models can be extrapolated to more complex models and geometries. Model performance is verified by comparing the numerical solutions to available analytical solutions.

This paper is organised as follows. Firstly, the different continuum elasticity theories with micro-inertia are presented in Section 2, including analytical solutions for the natural frequencies of several boundary conditions. Section 3 focuses on the spatial discretization of the corresponding continuum models, where different mass matrices are constructed. Section 4 contains a series of numerical tests and their results, with conclusions on their accuracy given in Section 5.

2. Elasticity theories with micro-inertia

Analytical solutions are derived for the natural frequencies of rod, Euler–Bernoulli beam, Rayleigh beam and membrane models equiped with micro-inertia. Although the *number* of boundary conditions of micro-inertia theories is typically the same as for classical elasticity (which is considered an advantage compared to higher-order strain gradient models), their *format* is still different from those of classical elasticity. For this reason, the models in this section will be given using variational principles, so that the consistent boundary conditions emerge automatically.

2.1. One-dimensional rod model

The Lagrangian $\mathcal{L}$ of the rod model extended with micro-inertia reads

$$\mathcal{L} = \int_0^L \left\{ \frac{1}{2}\rho \left[\left(\frac{\partial u}{\partial t}\right)^2 + \ell^2 \left(\frac{\partial^2 u}{\partial x \partial t}\right)^2 \right] - \frac{1}{2} E \left(\frac{\partial u}{\partial x}\right)^2 \right\} \mathrm{d}x \tag{1}$$

where E and ρ are the Young's modulus and the mass density, L is the length of the rod, while u is the longitudinal displacement, and x and t denote space and time, respectively. The additional inertia term in Eq. (1) is accompanied by a length scale parameter ℓ, which is a representation of the characteristic length of the material's microstructure. Applying Hamilton's Principle, the following governing equation is obtained

$$E\frac{\partial^2 u}{\partial x^2} - \rho\left(\frac{\partial^2 u}{\partial t^2} - \ell^2 \frac{\partial^4 u}{\partial x^2 \partial t^2}\right) = 0 \tag{2}$$

together with the boundary conditions, assumed to be homogeneous, given by

$$u = 0 \quad \text{or} \quad E\frac{\partial u}{\partial x} + \rho \ell^2 \frac{\partial^3 u}{\partial x \partial t^2} = 0 \tag{3}$$

Note that the natural boundary condition of Eq. (3) differs from the classical one unless $\ell = 0$: thus, the number of boundary conditions is the same as for classical elasticity, but their mathematical format has changed.

Analytical solutions for the natural frequencies ω_m and mode shapes $U_m(x)$ can be found via separation of variables. For a rod with two fixed ends the results are straightforwardly found as

$$\omega_m = \sqrt{\frac{E/\rho}{\left(\frac{m\pi}{L}\right)^{-2} + \ell^2}} \quad \text{and} \quad U_m(x) = C_m \sin\left(\frac{m\pi x}{L}\right) \tag{4}$$

and for the fixed-free rod we obtain

$$\omega_m = \sqrt{\frac{E/\rho}{\left(\frac{(2m-1)\pi}{2L}\right)^{-2} + \ell^2}} \quad \text{and}$$
$$U_m(x) = C_m \sin\left(\frac{(2m-1)\pi x}{2L}\right), \tag{5}$$

where $m \in \mathbb{N}^+$ is the mode number and C_m is the amplitude.

2.2. One-dimensional beam models

The Euler–Bernoulli theory for thin beams is widely employed in static problems. However, this theory shows unbounded propagation velocity for short wavelengths, an anomaly that can be avoided by Rayleigh theory [53]. Here, micro-inertia extensions of both the Euler–Bernoulli and Rayleigh beam models will be given first, after which these are used to calculate the natural frequencies for a variety of boundary conditions.

2.2.1. Euler–Bernoulli beam theory

The Lagrangian of an Euler–Bernoulli beam, extended with micro-inertia, can be written as

$$\mathcal{L} = \int_0^L \left\{ \frac{1}{2}\rho A \left[\left(\frac{\partial v}{\partial t}\right)^2 + \ell^2 \left(\frac{\partial^2 v}{\partial x \partial t}\right)^2 + \ell^4 \left(\frac{\partial^3 v}{\partial x^2 \partial t}\right)^2 \right] - \frac{1}{2} EI \left(\frac{\partial^2 v}{\partial x^2}\right)^2 \right\} \mathrm{d}x \tag{6}$$

where A and I are the cross-sectional area and the second moment of area, and v is the transverse displacement variable. Note that Eq. (6) includes two non-classical terms; in [28] it is shown how continuum models with higher-order inertia can be derived via the continualization of a lattice system, thereby linking the length scale parameters of the obtained continuum to the geometry of the lattice.

Applying Hamilton's Principle leads to a governing equation written as

$$EI\frac{\partial^4 v}{\partial x^4} + \rho A\left(\frac{\partial^2 v}{\partial t^2} - \ell^2 \frac{\partial^4 v}{\partial x^2 \partial t^2} + \ell^4 \frac{\partial^6 v}{\partial x^4 \partial t^2}\right) = 0 \tag{7}$$

with boundary conditions

$$v = 0 \quad \text{or} \quad EI\frac{\partial^3 v}{\partial x^3} - \rho A\left(\ell^2 \frac{\partial^3 v}{\partial x \partial t^2} - \ell^4 \frac{\partial^5 v}{\partial x^3 \partial t^2}\right) = 0 \tag{8}$$

and

$$\frac{\partial v}{\partial x} = 0 \quad \text{or} \quad EI\frac{\partial^2 v}{\partial x^2} + \rho A\ell^4 \frac{\partial^4 v}{\partial x^2 \partial t^2} = 0 \tag{9}$$

Again, the number of boundary conditions is the same as for the classical Euler–Bernoulli theory.

2.2.2. Rayleigh beam theory

The classical Rayleigh beam theory is similar to the classical Euler–Bernoulli one but for the incorporation of the rotary inertia of the cross-section. The Lagrangian of Rayleigh beam theory extended with micro-inertia is written as

$$\mathcal{L} = \int_0^L \left\{ \frac{1}{2}\rho A\left[\left(\frac{\partial v}{\partial t}\right)^2 + \ell^2\left(\frac{\partial^2 v}{\partial x \partial t}\right)^2\right] + \frac{1}{2}\rho I\left[\left(\frac{\partial^2 v}{\partial x \partial t}\right)^2 + \ell^2\left(\frac{\partial^3 v}{\partial x^2 \partial t}\right)^2\right] - \frac{1}{2}EI\left(\frac{\partial^2 v}{\partial x^2}\right)^2 \right\} \mathrm{d}x \tag{10}$$

Note that Eq. (10) has been chosen following the same criteria as that of the Euler–Bernoulli model, namely increasing the spatial order of the classical kinetic energy up to the same order as the classical potential one. Application of Hamilton's Principle then yields

$$EI\frac{\partial^4 v}{\partial x^4} + \rho A\frac{\partial^2 v}{\partial t^2} - \rho\left(I + A\ell^2\right)\frac{\partial^4 v}{\partial x^2 \partial t^2} + \rho I\ell^2 \frac{\partial^6 v}{\partial x^4 \partial t^2} = 0 \tag{11}$$

where the associated boundary conditions are found as

$$v = 0 \quad \text{or} \quad EI\frac{\partial^3 v}{\partial x^3} - \rho\left(I + A\ell^2\right)\frac{\partial^3 v}{\partial x \partial t^2} + \rho I\ell^2 \frac{\partial^5 v}{\partial x^3 \partial t^2} = 0 \tag{12}$$

together with

$$\frac{\partial v}{\partial x} = 0 \quad \text{or} \quad EI\frac{\partial^2 v}{\partial x^2} + \rho I\ell^2 \frac{\partial^4 v}{\partial x^2 \partial t^2} = 0 \tag{13}$$

2.2.3. Natural frequencies

Employing separation of variables according to $v(x,t) = V(x)e^{i\omega t}$ results in

$$\frac{\partial^4 V}{\partial x^4} + \kappa\frac{\partial^2 V}{\partial x^2} - \gamma V = 0 \tag{14}$$

where

$$\kappa = \frac{\rho A\ell^2\omega^2}{EI - \rho A\ell^4\omega^2} \quad \text{and} \quad \gamma = \frac{\rho A\omega^2}{EI - \rho A\ell^4\omega^2} \tag{15}$$

for Euler–Bernoulli theory with micro-inertia and

$$\kappa = \frac{\rho\left(I + A\ell^2\right)\omega^2}{EI - \rho I\ell^2\omega^2} \quad \text{and} \quad \gamma = \frac{\rho A\omega^2}{EI - \rho I\ell^2\omega^2} \tag{16}$$

for Rayleigh theory with micro-inertia. Hence, the general solution of Eq. (14) reads

$$V(x) = c_1\cos(\psi x) + c_2\sin(\psi x) + c_3\cosh(\phi x) + c_4\sinh(\phi x) \tag{17}$$

where

$$\psi = \sqrt{\frac{\sqrt{\kappa^2 + 4\gamma} + \kappa}{2}} \quad \text{and} \quad \phi = \sqrt{\frac{\sqrt{\kappa^2 + 4\gamma} - \kappa}{2}} \tag{18}$$

Furthermore, c_1, c_2, c_3 and c_4 are arbitrary constants that can be obtained by imposing four boundary conditions as detailed in Appendix A for a simply supported beam and for a cantilever beam. Afterwards, natural frequencies can be obtained from the characteristic equation of the homogeneous system.

2.3. Two-dimensional membrane model

Finally, the micro-inertia version of the two-dimensional membrane model is studied. Assuming a rectangular domain with dimensions L_x and L_y, the Lagrangian of this model is given by

$$\mathcal{L} = \int_0^{L_x}\int_0^{L_y} \left\{ \frac{1}{2}\rho\left[\left(\frac{\partial v}{\partial t}\right)^2 + \ell^2\left(\frac{\partial^2 v}{\partial x \partial t}\right)^2 + \ell^2\left(\frac{\partial^2 v}{\partial y \partial t}\right)^2\right] - \frac{1}{2}T\left[\left(\frac{\partial v}{\partial x}\right)^2 + \left(\frac{\partial v}{\partial y}\right)^2\right] \right\} \mathrm{d}y\mathrm{d}x \tag{19}$$

where T is an in-plane tensile load, v is the out-of-plane displacement and ρ is the mass per unit of area. Hence, applying Hamilton's Principle gives

$$T\left(\frac{\partial^2 v}{\partial x^2} + \frac{\partial^2 v}{\partial y^2}\right) - \rho\left[\frac{\partial^2 v}{\partial t^2} - \ell^2\left(\frac{\partial^4 v}{\partial x^2 \partial t^2} + \frac{\partial^4 v}{\partial y^2 \partial t^2}\right)\right] = 0 \tag{20}$$

with the boundary conditions

$$v = 0 \tag{21}$$

or

$$T\left(\frac{\partial v}{\partial x}\cdot n_x + \frac{\partial v}{\partial y}\cdot n_y\right) + \rho\ell^2\left(\frac{\partial^3 v}{\partial x \partial t^2}\cdot n_x + \frac{\partial^3 v}{\partial y \partial t^2}\cdot n_y\right) = 0 \tag{22}$$

where n_x and n_y are the components of the normal vector of the domain surface ∂S.

Separation of variables is applied through $v(x,y,t) = X(x)Y(y)e^{i\omega t}$, so that

$$T\left(\frac{\partial^2 X}{\partial x^2}Y + X\frac{\partial^2 Y}{\partial y^2}\right) + \rho\omega^2\left[XY - \ell^2\left(\frac{\partial^2 X}{\partial x^2}Y + X\frac{\partial^2 Y}{\partial y^2}\right)\right] = 0 \tag{23}$$

from which it can be found that

$$\frac{1}{X}\frac{\partial^2 X}{\partial x^2} = -\frac{1}{Y}\frac{\partial^2 Y}{\partial y^2} - \frac{\rho\omega^2}{T - \rho\ell^2\Omega^2} \equiv -k_x^2 \tag{24}$$

or, equivalently,

$$\frac{1}{Y}\frac{\partial^2 Y}{\partial y^2} = -\frac{1}{X}\frac{\partial^2 X}{\partial x^2} - \frac{\rho\omega^2}{T - \rho\ell^2\omega^2} \equiv -k_y^2 \tag{25}$$

where the constants k_x and k_y are related through

$$k_x^2 + k_y^2 = \frac{\rho\omega^2}{T - \rho\ell^2\omega^2} \tag{26}$$

Thus, the following solutions for $X(x)$ and $Y(y)$ are found:

$$X(x) = a_1\cos(k_x x) + a_2\sin(k_x x) \tag{27}$$

$$Y(y) = b_1\cos(k_y y) + b_2\sin(k_y y). \tag{28}$$

where a_1, a_2, b_1 and b_2 are constants to be determined via the boundary conditions. The most common configuration for a membrane is fixed along all edges. This leads to $a_1 = b_1 = 0$ together with

$$k_x = \frac{m\pi}{L_x} \quad \text{and} \quad k_y = \frac{n\pi}{L_y} \tag{29}$$

with $m, n \in \mathbb{N}^+$. Therefore, the natural frequency for mode (m, n) is given through

$$\omega_{m,n} = \sqrt{\frac{T\left(\frac{m^2\pi^2}{L_x^2} + \frac{n^2\pi^2}{L_y^2}\right)}{\rho\left[1 + \ell^2\left(\frac{m^2\pi^2}{L_x^2} + \frac{n^2\pi^2}{L_y^2}\right)\right]}} \tag{30}$$

while the associated mode shape is expressed as

$$V_{m,n}(x,y) \equiv X(x)Y(y) = C_{m,n} \sin\left(\frac{m\pi x}{L_x}\right) \sin\left(\frac{n\pi x}{L_y}\right) \tag{31}$$

3. Spatial discretization aspects

The analytical solutions for the natural frequencies and mode shapes given above will serve as reference solutions for the associated finite element solutions. After spatial discretization of the relevant governing equations, the element equations can be written generically in modal form as

$$\left[-\omega^2(\mathbf{M} + \mathbf{M}_\ell) + \mathbf{K}\right]\mathbf{d} = 0 \tag{32}$$

where $\mathbf{M}$ and $\mathbf{K}$ are the standard mass and stiffness matrices, while $\mathbf{M}_\ell$ is the mass matrix associated with the micro-inertia terms. Moreover, $\mathbf{d}$ contains the nodal degrees of freedom.

The matrices $\mathbf{K}$ and $\mathbf{M}_\ell$ are typically given non-ambiguously for each model and therefore cannot be modified. In that context, note that it is not possible to lump $\mathbf{M}_\ell$ without losing the micro-inertia properties of the model. Hence, the system matrix as given above is not diagonal – but see [54,55] for a discussion of these issues and solution strategies.

On the other hand, the classical mass matrix $\mathbf{M}$ can be constructed in different ways without affecting the overall mass properties of the model, thus allowing the system matrix to be modified in order to maximise accuracy. In particular, the *consistent mass matrix* assumes a distribution of the mass over the entire element and makes use of the same shape functions as those employed to develop the stiffness matrix, while a *lumped mass matrix* is obtained by assuming that the total mass of the elements is distributed at the nodes. In addition, Hughes [56] demonstrated that, for classical models, a linear combination of consistent and lumped mass matrices may results in a more accurate numerical model. This linear combination is denoted as the *higher-order* mass matrix and defined via

$$\mathbf{M}_\mathrm{H} = \alpha\mathbf{M}_\mathrm{C} + (1-\alpha)\mathbf{M}_\mathrm{L} \quad \text{with} \quad 0 \leqslant \alpha \leqslant 1 \tag{33}$$

where $\mathbf{M}_\mathrm{C}, \mathbf{M}_\mathrm{L}$ and $\mathbf{M}_\mathrm{H}$ denote the consistent, lumped and higher-order mass matrix, respectively. Furthermore, α is a constant that can be set by the user.

A pertinent question arises in the context of the present paper: *is it possible to find optimal values for α in the context of elasticity theories with micro-inertia?* To answer this question, the mass and stiffness matrices corresponding to the models studied in this work are summarised below.

3.1. One-dimensional rod model

The consistent and lumped mass matrices for a rod element are given by

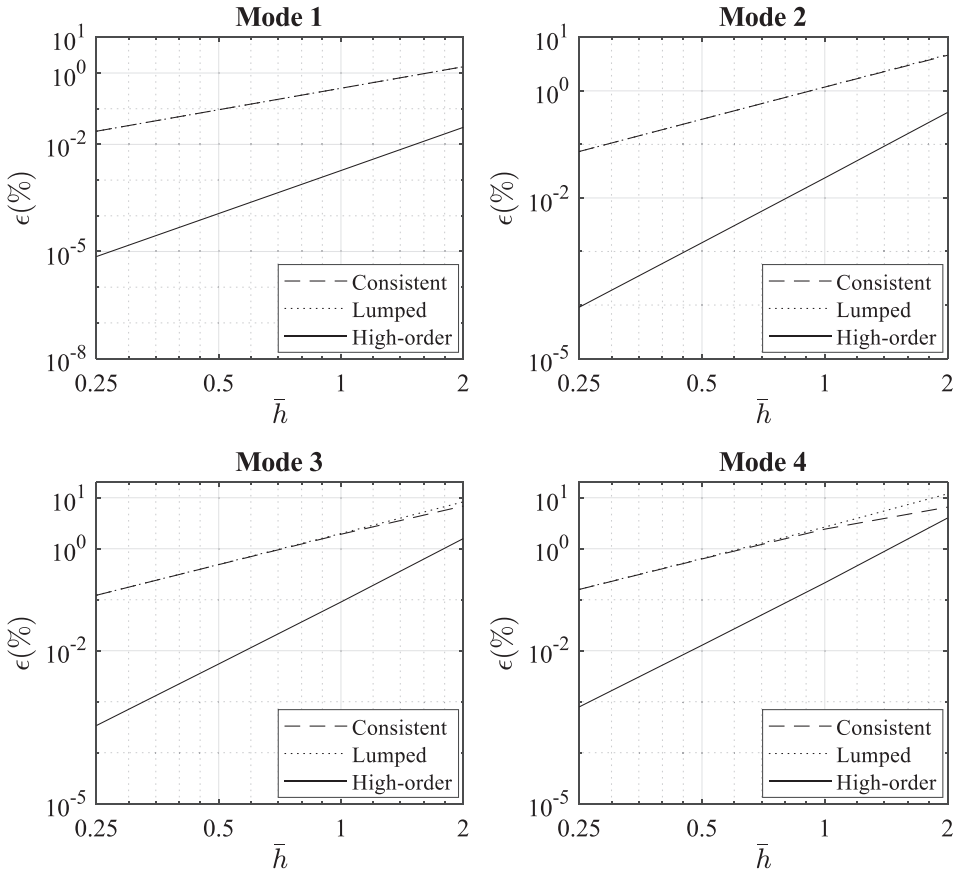

Fig. 1. Relative error versus element size for a fixed–fixed rod.

$$\mathbf{M}_{\mathrm{C}} = \rho h \begin{bmatrix} \frac{1}{3} & \frac{1}{6} \\ \frac{1}{6} & \frac{1}{3} \end{bmatrix} \quad \text{and} \quad \mathbf{M}_{\mathrm{L}} = \rho h \begin{bmatrix} \frac{1}{2} & 0 \\ 0 & \frac{1}{2} \end{bmatrix} \tag{34}$$

whereas the micro-inertia mass matrix and stiffness matrix read

$$\mathbf{M}_{\ell} = \frac{\rho \ell^2}{h} \begin{bmatrix} 1 & -1 \\ -1 & 1 \end{bmatrix} \quad \text{and} \quad \mathbf{K} = \frac{E}{h} \begin{bmatrix} 1 & -1 \\ -1 & 1 \end{bmatrix} \tag{35}$$

where throughout h denotes the size of the finite element. As shown in Eq. (33), the higher-order mass matrix of the rod model can be obtained by combining both consistent and lumped mass matrices. In Appendix B, it has been demonstrated that the most accurate value of α in this case is $\alpha = 0.5$, which leads to

$$\mathbf{M}_{\mathrm{H}} = \rho h \begin{bmatrix} \frac{5}{12} & \frac{1}{12} \\ \frac{1}{12} & \frac{5}{12} \end{bmatrix} \tag{36}$$

3.2. One-dimensional beam models

Standard cubic Hermite shape functions have been used for both beam theories studied in this paper.

3.2.1. Euler–Bernoulli beam theory

For an Euler–Bernoulli beam element, the consistent mass matrix is given by

$$\mathbf{M}_{\mathrm{C}} = \frac{\rho A h}{420} \begin{bmatrix} 156 & 22h & 54 & -13h \\ 22h & 4h^2 & 13h & -3h^2 \\ 54 & 13h & 156 & -22h \\ -13h & -3h^2 & -22h & 4h^2 \end{bmatrix} \tag{37}$$

whereas the micro-inertia mass matrix reads

$$\mathbf{M}_{\ell} = \frac{\rho A \ell^2}{30h} \begin{bmatrix} 36 & 3h & -36 & 3h \\ 3h & 4h^2 & -3h & -h^2 \\ -36 & -3h & 36 & -3h \\ 3h & -h^2 & -3h & 4h^2 \end{bmatrix} + \frac{\rho A \ell^4}{h^3} \begin{bmatrix} 12 & 6h & -12 & 6h \\ 6h & 4h^2 & -6h & 2h^2 \\ -12 & -6h & 12 & -6h \\ 6h & 2h^2 & -6h & 4h^2 \end{bmatrix} \tag{38}$$

Furthermore, the stiffness matrix is written as

$$\mathbf{K} = \frac{EI}{h^3} \begin{bmatrix} 12 & 6h & -12 & 6h \\ 6h & 4h^2 & -6h & 2h^2 \\ -12 & -6h & 12 & -6h \\ 6h & 2h^2 & -6h & 4h^2 \end{bmatrix} \tag{39}$$

The consistent mass matrix of Eq. (37) can be transformed into the lumped mass matrix by different procedures – an in-depth discussion can be found in [57]. Here, we will consider the lumped mass matrix obtained from the nodal integration technique [58]:

$$\mathbf{M}_{\mathrm{L}} = \frac{\rho A h}{2} \begin{bmatrix} 1 & 0 & 0 & 0 \\ 0 & 0 & 0 & 0 \\ 0 & 0 & 1 & 0 \\ 0 & 0 & 0 & 0 \end{bmatrix} \tag{40}$$

A straightforward expression for the higher-order mass matrix can be obtained directly from Eq. (33). Assuming again $\alpha = 0.5$, the following mass matrix is found and indicated with "higher-order I" in this paper:

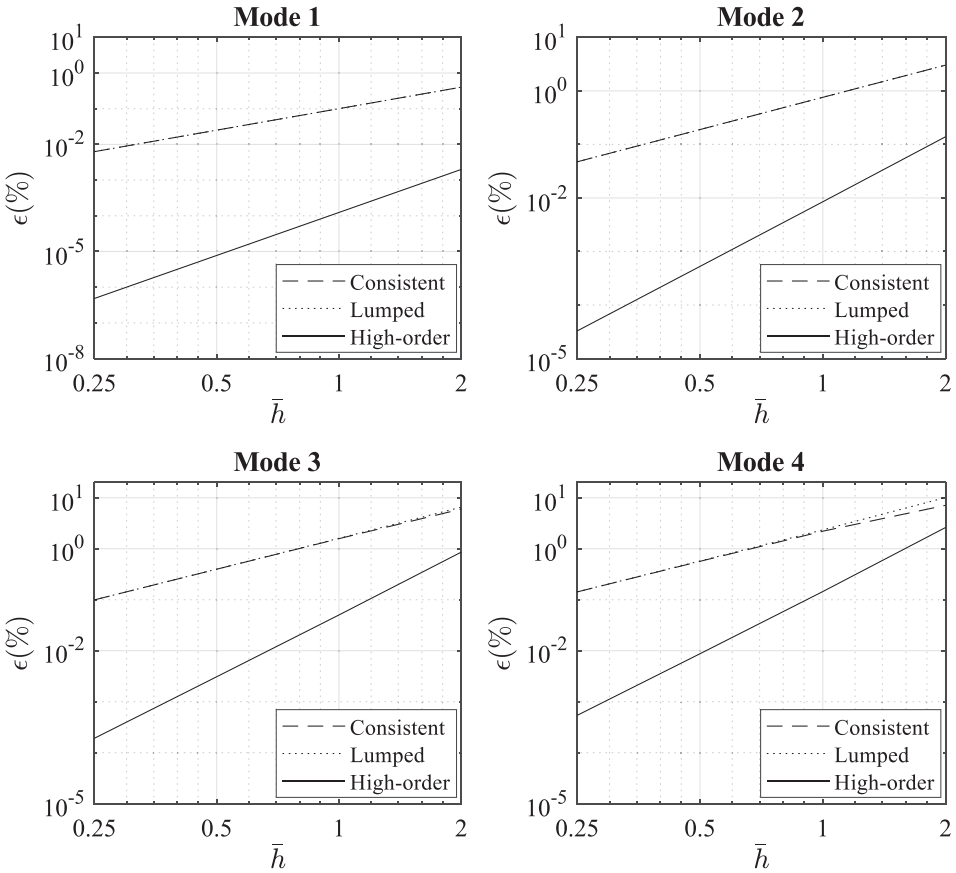

Fig. 2. Relative error versus element size for a fixed-free rod.

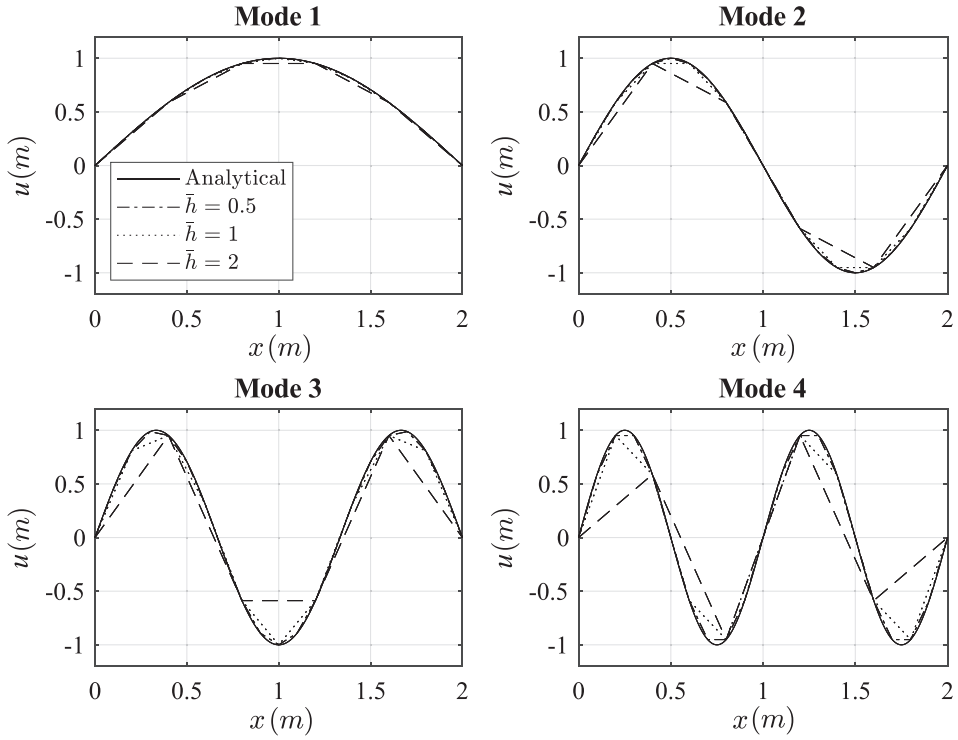

Fig. 3. Normalized mode shapes of a fixed–fixed rod with higher-order mass matrix.

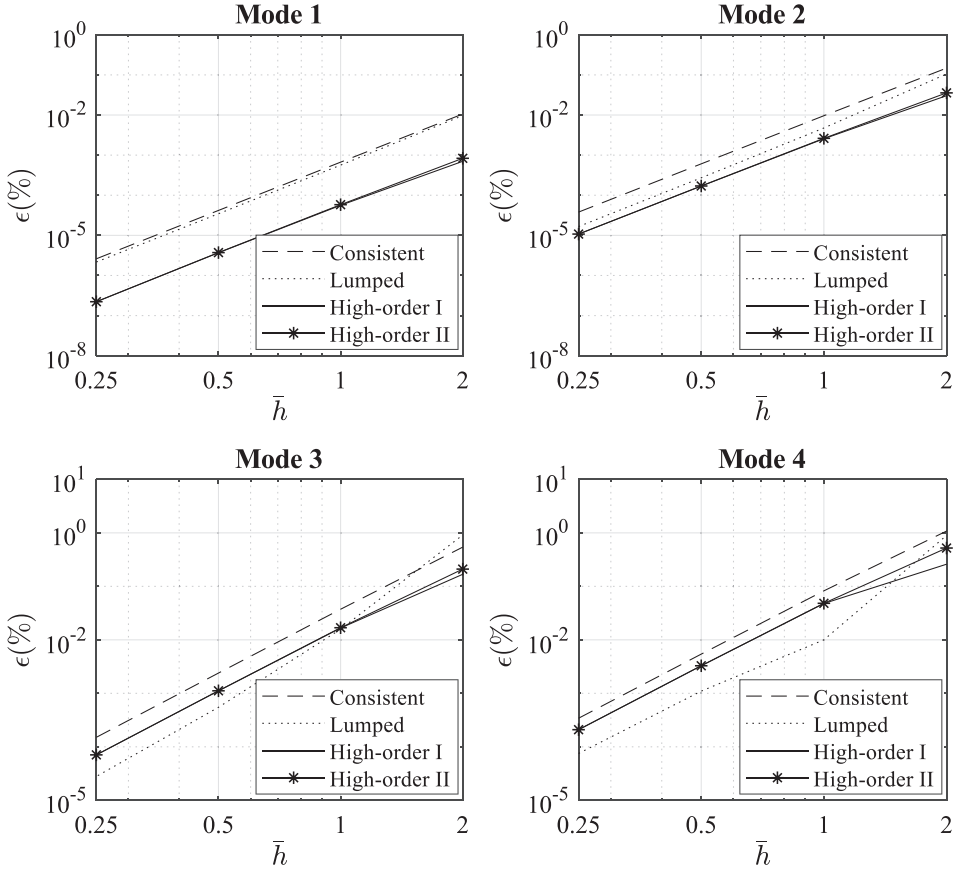

Fig. 4. Relative error versus element size for a simply supported Euler–Bernoulli beam.

$$\mathbf{M}_{\mathrm{H}}^{\mathrm{I}} = \frac{\rho A h}{840}\begin{bmatrix} 366 & 22h & 54 & -13h \\ 22h & 4h^2 & 13h & -3h^2 \\ 54 & 13h & 366 & -22h \\ -13h & -3h^2 & -22h & 4h^2 \end{bmatrix} \tag{41}$$

Alternatively, Hughes [56] proposed another higher-order mass matrix for classical beam models, obtained via a linear combination of the consistent mass matrix and the stiffness matrix:

$$\mathbf{M}_{\mathrm{H}}^{\mathrm{II}} = \mathbf{M}_{\mathrm{C}} + \frac{\rho A h^4}{720 E I}\mathbf{K} = \frac{\rho A h}{2520}\begin{bmatrix} 978 & 153h & 282 & -57h \\ 153h & 38h^2 & 57h & -11h^2 \\ 282 & 57h & 978 & -153h \\ -57h & -11h^2 & -153h & 38h^2 \end{bmatrix} \tag{42}$$

This higher-order mass matrix will be denoted as "higher-order II" in the remainder of this work.

3.2.2. Rayleigh beam model

A finite element derived from Rayleigh beam theory has a consistent mass matrix consisting of two parts, related to translational and rotary inertia, respectively:

$$\mathbf{M}_{\mathrm{C}} = \frac{\rho A h}{420}\begin{bmatrix} 156 & 22h & 54 & -13h \\ 22h & 4h^2 & 13h & -3h^2 \\ 54 & 13h & 156 & -22h \\ -13h & -3h^2 & -22h & 4h^2 \end{bmatrix} + \frac{\rho I}{30h}\begin{bmatrix} 36 & 3h & -36 & 3h \\ 3h & 4h^2 & -3h & -h^2 \\ -36 & -3h & 36 & -3h \\ 3h & -h^2 & -3h & 4h^2 \end{bmatrix} \tag{43}$$

The associated micro-inertia mass matrix similarly has two contributions:

$$\mathbf{M}_{\ell} = \frac{\rho A \ell^2}{30h}\begin{bmatrix} 36 & 3h & -36 & 3h \\ 3h & 4h^2 & -3h & -h^2 \\ -36 & -3h & 36 & -3h \\ 3h & -h^2 & -3h & 4h^2 \end{bmatrix} + \frac{\rho I \ell^2}{h^3}\begin{bmatrix} 12 & 6h & -12 & 6h \\ 6h & 4h^2 & -6h & 2h^2 \\ -12 & -6h & 12 & -6h \\ 6h & 2h^2 & -6h & 4h^2 \end{bmatrix} \tag{44}$$

The element stiffness matrix of Rayleigh beam theory is identical to that of Euler–Bernoulli beam theory, cf. Eq. (39). To obtain a lumped mass matrix, nodal integration is used again, which yields

$$\mathbf{M}_{\mathrm{L}} = \frac{\rho A h}{2}\begin{bmatrix} 1 & 0 & 0 & 0 \\ 0 & 0 & 0 & 0 \\ 0 & 0 & 1 & 0 \\ 0 & 0 & 0 & 0 \end{bmatrix} + \frac{\rho I h}{2}\begin{bmatrix} 0 & 0 & 0 & 0 \\ 0 & 1 & 0 & 0 \\ 0 & 0 & 0 & 0 \\ 0 & 0 & 0 & 1 \end{bmatrix} \tag{45}$$

Finally, following the same approach as for Euler–Bernoulli theory, the following higher-order mass matrices are obtained:

$$\mathbf{M}_{\mathrm{H}}^{\mathrm{I}} = \frac{\rho A h}{840}\begin{bmatrix} 366 & 22h & 54 & -13h \\ 22h & 4h^2 & 13h & -3h^2 \\ 54 & 13h & 366 & -22h \\ -13h & -3h^2 & -22h & 4h^2 \end{bmatrix} + \frac{\rho I}{60h}\begin{bmatrix} 36 & 3h & -36 & 3h \\ 3h & 19h^2 & -3h & -h^2 \\ -36 & -3h & 36 & -3h \\ 3h & -h^2 & -3h & 19h^2 \end{bmatrix} \tag{46}$$

and

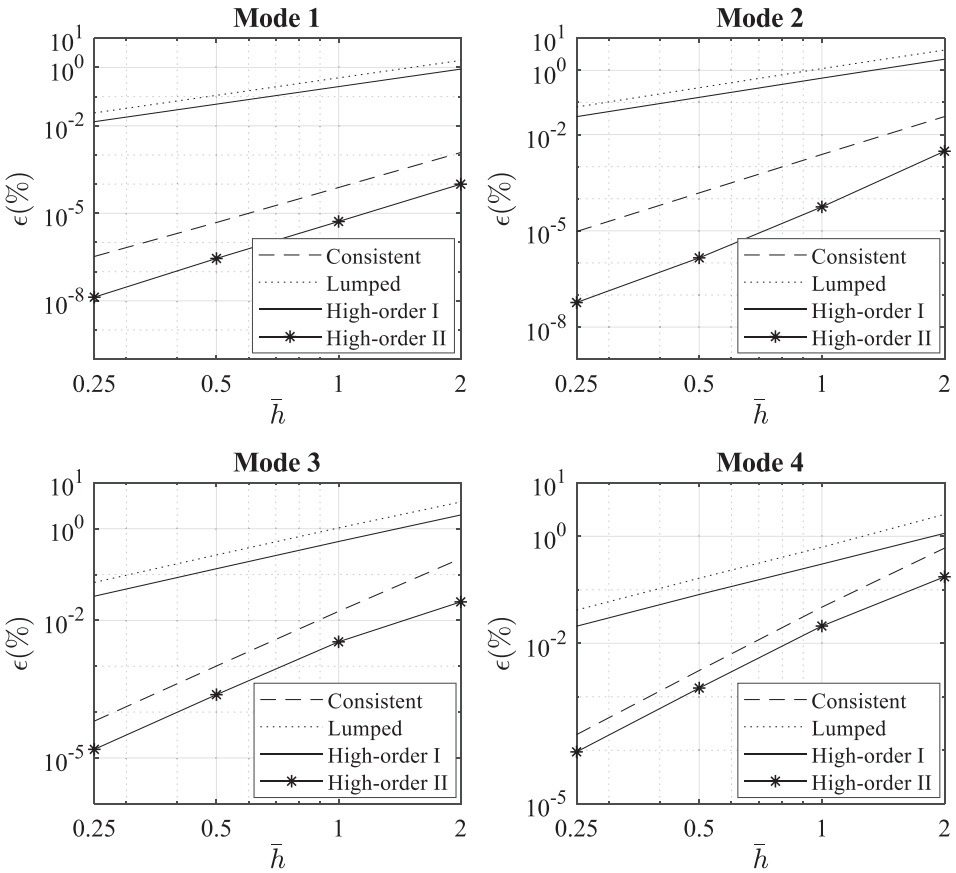

Fig. 5. Relative error versus element size for a cantilever Euler–Bernoulli beam.

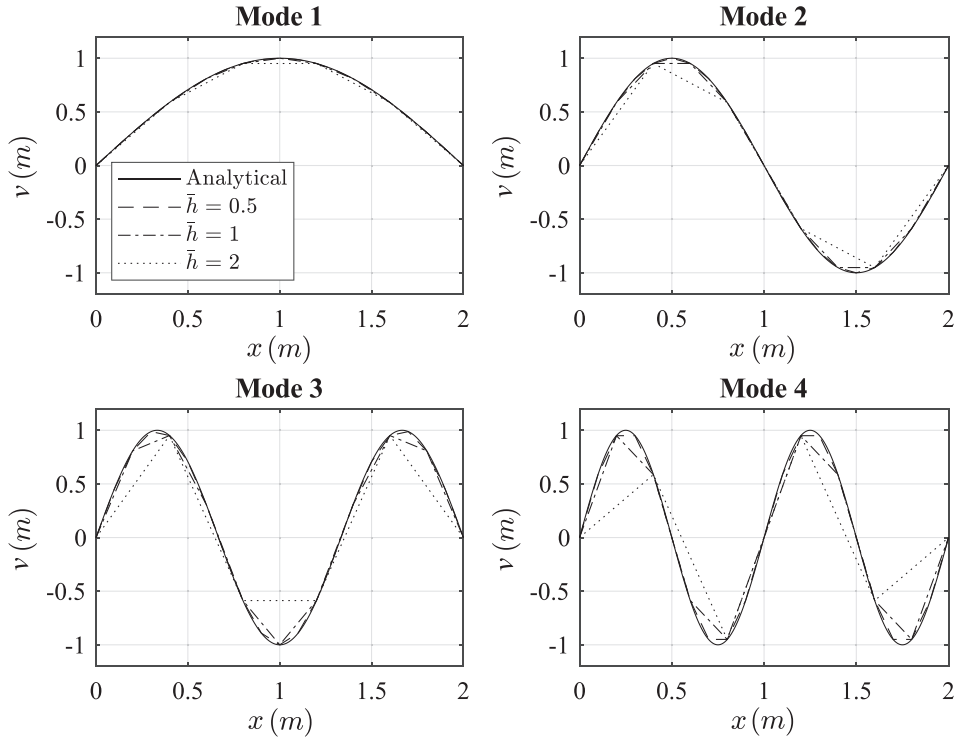

Fig. 6. Normalized mode shapes of a simply supported Euler–Bernoulli beam with higher-order II mass matrix.

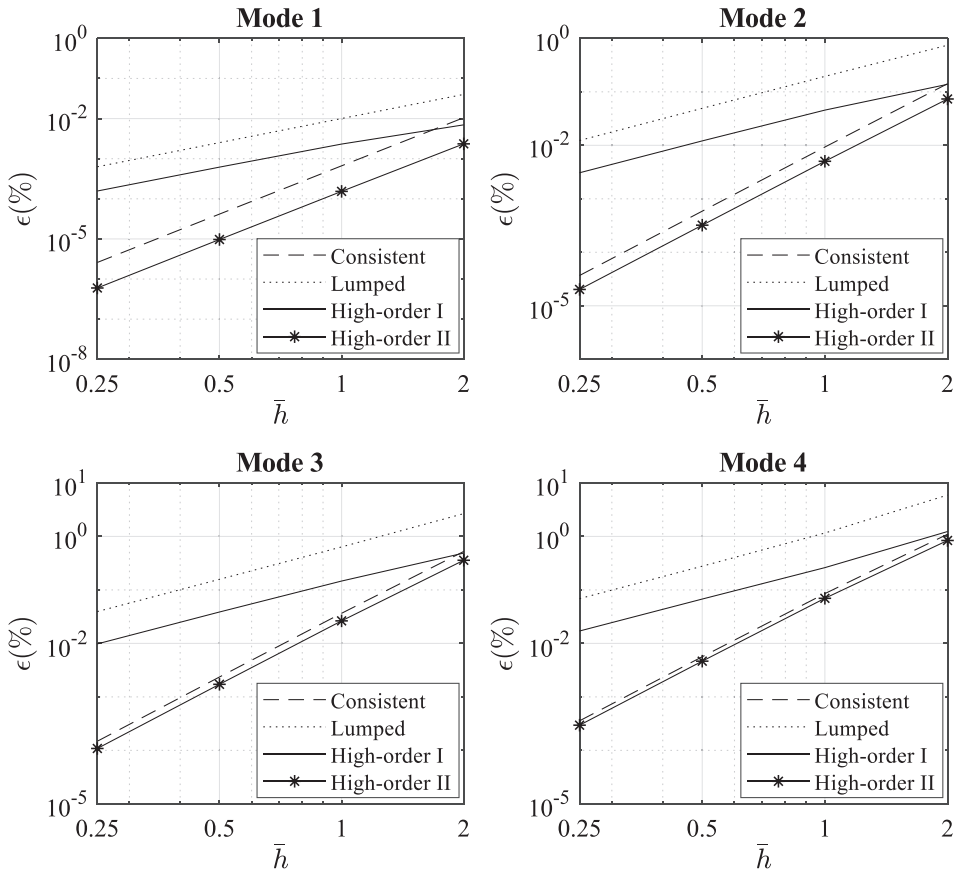

Fig. 7. Relative error versus element size for a simply supported Rayleigh beam.

$$\mathbf{M}_{\mathrm{H}}^{\mathrm{II}} = \frac{\rho A h}{2520}\begin{bmatrix} 978 & 153h & 282 & -57h \\ 153h & 38h^2 & 57h & -11h^2 \\ 282 & 57h & 978 & -153h \\ -57h & -11h^2 & -153h & 38h^2 \end{bmatrix} + \frac{\rho I}{30h}\begin{bmatrix} 36 & 3h & -36 & 3h \\ 3h & 4h^2 & -3h & -h^2 \\ -36 & -3h & 36 & -3h \\ 3h & -h^2 & -3h & 4h^2 \end{bmatrix} \tag{47}$$

3.3. Two-dimensional membrane model

Next, the finite element equations associated with Eq. (20) will be developed. To this end, a weak form is formulated by multiplying Eq. (20) with a weight function δv and integrating the result over the domain Ω. Applying the divergence theorem yields

$$\begin{aligned} &\int_\Omega(\delta v \rho v_{tt})d\Omega + \int_\Omega(\delta v_x T v_x + \delta v_y T v_y)d\Omega \\ &\quad + \int_\Omega(\delta v_x \rho \ell^2 v_{xtt} + \delta v_y \rho \ell^2 v_{ytt})d\Omega \\ &= \int_{\partial\Omega}(\delta v(T v_x \cdot n_x + T v_y \cdot n_y))dS \\ &\quad + \int_{\partial\Omega}(\delta v \rho \ell^2 (T v_{xtt} \cdot n_x + T v_{ytt} \cdot n_y))dS \end{aligned} \tag{48}$$

The surface of the membrane $\Omega \equiv L_x L_y$. Thus, the following mass and stiffness matrices are found

$$\mathbf{M}_{\mathrm{C}} = \rho \int_\Omega \mathbf{N}^T N d\boldsymbol{\Omega} \tag{49}$$

$$\mathbf{M}_\ell = \rho \ell^2 \int_\Omega \left(\frac{\partial \mathbf{N}^T}{\partial x}\frac{\partial \mathbf{N}}{\partial x} + \frac{\partial \mathbf{N}^T}{\partial y}\frac{\partial \mathbf{N}}{\partial y}\right) d\boldsymbol{\Omega} \tag{50}$$

and

$$\mathbf{K} = T \int_\Omega \left(\frac{\partial \mathbf{N}^T}{\partial x}\frac{\partial \mathbf{N}}{\partial x} + \frac{\partial \mathbf{N}^T}{\partial y}\frac{\partial \mathbf{N}}{\partial y}\right) d\boldsymbol{\Omega} \tag{51}$$

where $\mathbf{N}$ contains the shape functions. Note that the micro-inertia mass matrix is a scalar multiple of the stiffness matrix.

The lumped mass matrix can be obtained straightforwardly from the consistent mass matrix via the row-sum technique, e.g. Two different higher-order mass matrices will be studied for the membrane model, taking either $\alpha = \frac{1}{2}$ or $\alpha = \frac{3}{4}$ in Eq. (33); these will be indicated as "higher-order I" and "higher-order II" mass matrices, respectively.

4. Discussion of results

In this section, the natural frequencies obtained by the numerical methods will be compared with those provided by the analytical solutions. Different vibration modes will be evaluated, presenting the relative errors corresponding to each employed mass matrix, as a function of the normalised element size $\overline{h} \equiv h/\ell$. The relative error ϵ is defined in terms of the natural frequency as

$$\epsilon = \frac{|\omega_{\text{analytical}} - \omega_{\text{numerical}}|}{\omega_{\text{analytical}}} \times 100\% \tag{52}$$

A double logarithmic scale is adopted in the associated Figures in order to be able to verify whether the convergence rate, upon mesh refinement, of the numerical solutions matches the theoretical convergence rate.

As explained above, the continuum models with micro-inertia are able to capture the scale effects through space–time cross

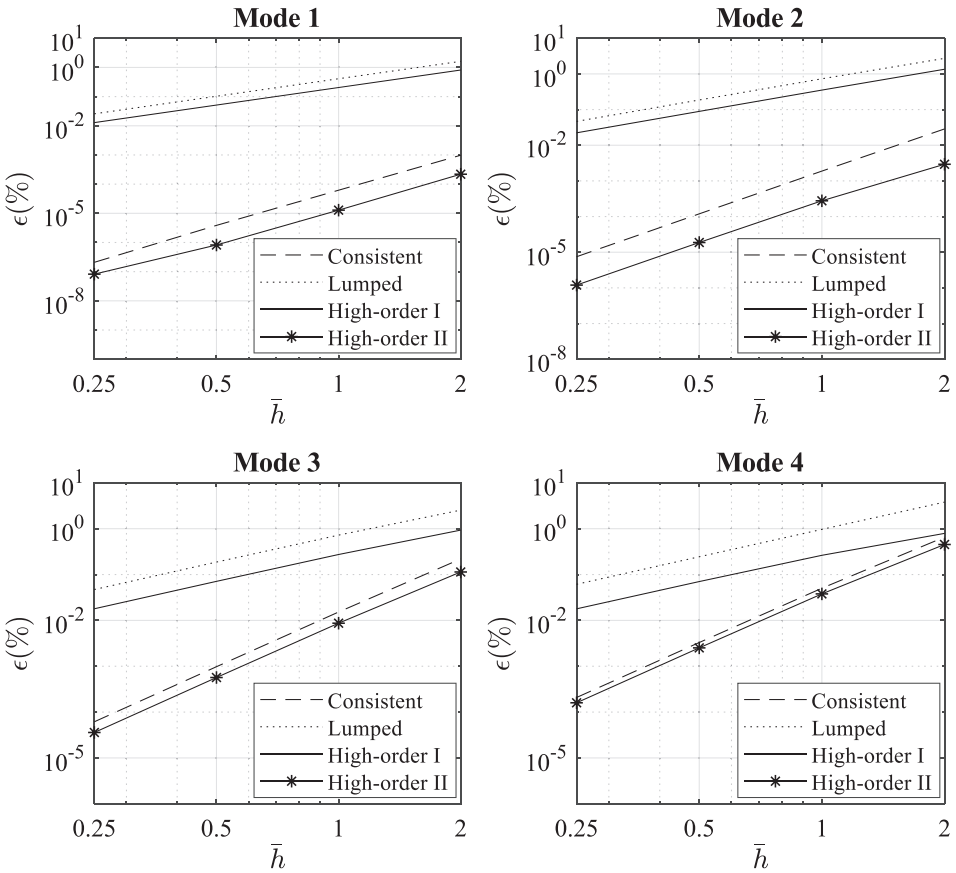

Fig. 8. Relative error versus element size for a cantilever Rayleigh beam.

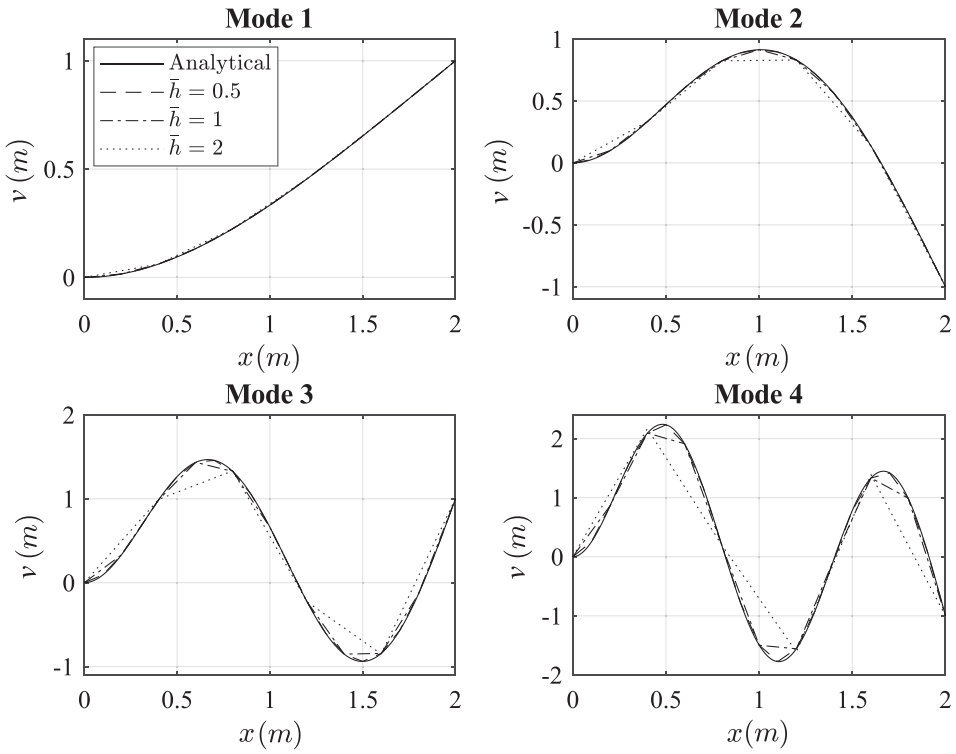

Fig. 9. Normalized mode shapes of a cantilever Rayleigh beam with higher-order II mass matrix.

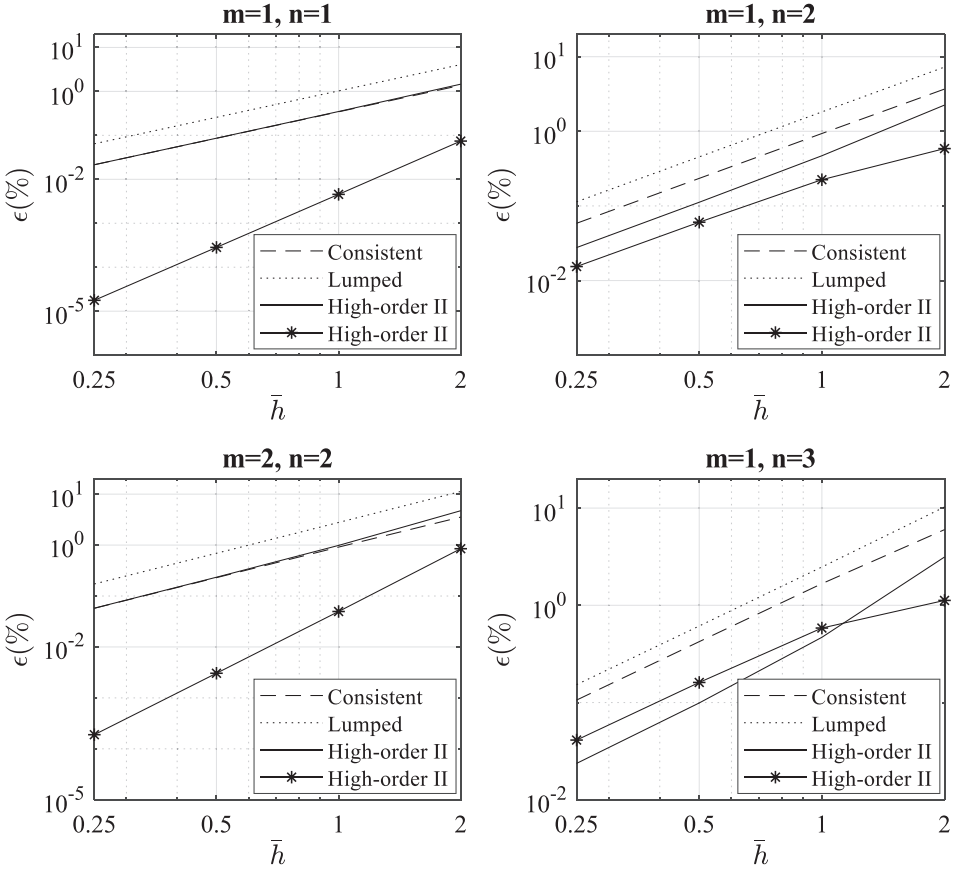

Fig. 10. Relative error versus element size for a square membrane.

derivatives that are accompanied by the length scale ℓ, hence the scale effects become less significant as ℓ tends to zero. Where natural frequencies are concerned, the relevance of the scale effects depends on the ratio between ℓ and the wave length of the vibration mode. To study this systematically, a ratio of $\mu = L/\ell = 10$ has been considered with L the length of the rod, length of the beam, or the edge length of a square membrane. Considering this value for μ, the scale effects arise even for the lowest modes. The relevance of scale effects for such a ratio can be observed in [26,28,36] for rods, beams and membranes, respectively.

4.1. One-dimensional rod model

As an illustrative example, we consider here a rod with the following properties: $L = 2$ m, $E = 70$ GPa, $\rho = 3000$ kg/m^3 and $\ell = 0.2$ m. Figs. 1 and 2 show the relative errors of the natural frequencies corresponding to the first four modes of the fixed–fixed and fixed-free configurations, respectively. For both configurations, and for all considered modes, the higher-order mass matrix leads to (i) significantly lower errors and (ii) a higher convergence rate than both the consistent mass matrix and the lumped mass matrix. Note that with the higher-order mass matrix the natural frequencies can be obtained with good accuracy using an element size of twice the length scale (i.e. $\overline{h} = 2$), with the fourth mode presenting an error lower than 4%, and even lower errors for the lower modes. In Fig. 3 the mode shapes of the first four modes have been plotted, comparing the numerical results of the higher-order mass matrix with the analytical solution of Eq. (4). It is clear that higher modes require smaller element sizes. Nevertheless, the first four modes can be attained with considerable reliability taking $\overline{h} \leqslant 1$.

4.2. One-dimensional beam models

Next, the results obtained from both Euler–Bernoulli and Rayleigh beam models will be analysed. A beam with the following properties is considered: $L = 2$ m, $E = 70$ GPa, $\rho = 3000$ kg/m^3, $A = 0.1$ m^2, $I = 1/120$ m^4 and $\ell = 0.2$ m.

4.3. Euler–Bernoulli theory

Figs. 4 and 5 show the relative errors of the first four natural frequencies for a simply supported and a cantilever Euler–Bernoulli beam, respectively. It can be seen in Fig. 4 that, for the simply supported beam, all four mass matrices show similar convergence rates whereby halving the element size leads to a roughly tenfold decrease in relative error. For this particular example, there does not seem to be much added value in using a higher-order mass matrix – although it does not seem to be disadvantageous either.

Conversely, the results of the cantilever beam plotted in Fig. 5 show a signficant difference between the two higher-order mass matrices. The convergence rate of the higher-order II mass matrix is superior to those of the lumped mass matrix and the higher-order I mass matrix, but also somewhat better than that of the consistent mass matrix. Comparing these results with those of the Rayleigh theory given in the next section, it seems that the results of Fig. 4 are the outlier, not those of Fig. 5: the lumped mass matrix and the higher-order I matrix appear to demonstrate superconvergent behaviour in Fig. 4 compared to all the other results with the same matrices. However, considering the totality of the results, the higher-order II matrix is clearly the preferred option.

Finally, note that when the higher-order II mass matrix is used, the natural frequencies are obtained with high accuracy even with an element size twice the magnitude of the physical length scale (i.e. $\overline{h} = 2$) – cf. the fourth natural frequency exhibiting an error less than 0.5% for both sets of support conditions. Fig. 6 shows the mode shapes of the first four modes of a simply supported beam, employing the higher-order II mass matrix. Similar to the results of Fig. 3, relative element sizes $\overline{h} \leqslant 1$ are required to give a reasonable approximation of the first four mode shapes – this similarity is due to the fact that Eqns. (4) and (A.5) are formally equivalent.

4.4. Rayleigh theory

Figs. 7 and 8 show the relative errors of the natural frequencies corresponding to simply supported and cantilever Rayleigh beams, respectively. The results are consistent (and in line with the results for the Euler–Bernoulli cantilever beam): the higher-order II mass matrix shows the best performance in terms of convergence rate and in terms of absolute error the consistent mass matrix leads to a similar convergence rate but a higher absolute error, whereas

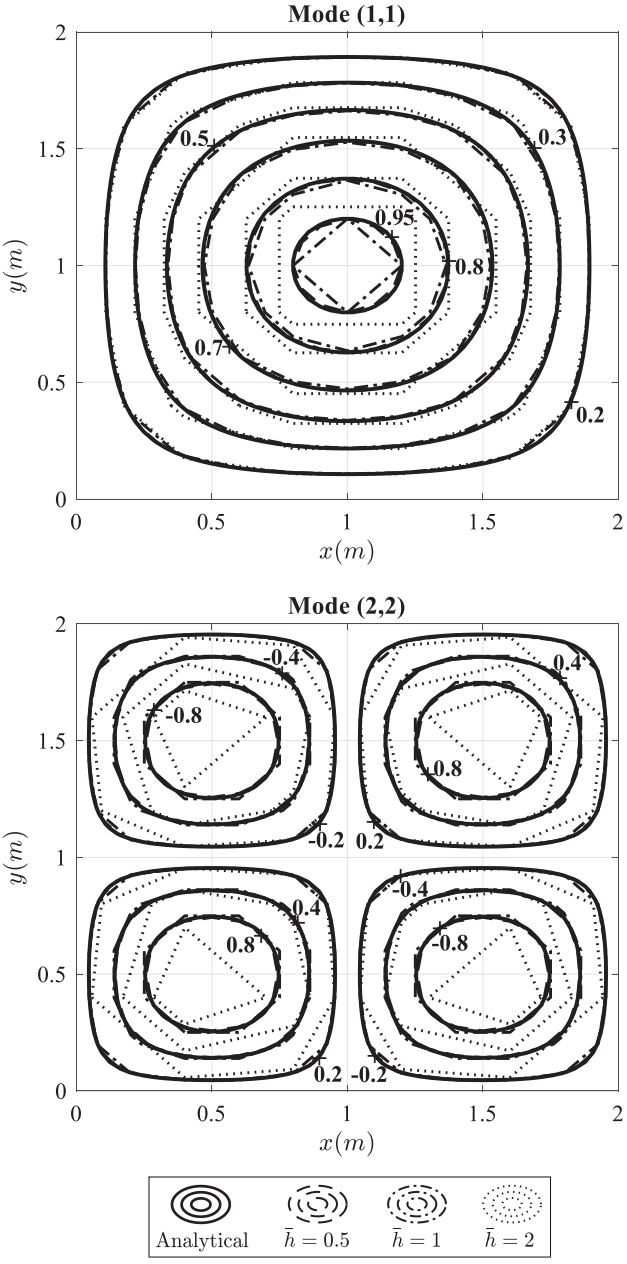

Fig. 11. Normalized mode shapes of modes $(1,1)$ and $(2,2)$ of a square membrane with higher-order I mass matrix.

use of the higher-order I mass matrix and the lumped mass matrix leads to slower convergence rates. Furthermore, the higher-order II mass matrix captures all four natural frequencies within 1% error with a relative element size $\overline{h} = 2$.

Finally, the mode shapes of the first four modes of the cantilever beam are plotted in Fig. 9, employing the higher-order II mass matrix of the Rayleigh model (the mode shapes of the simply supported beam are similar to those of the Euler–Bernoulli case and thus not shown here). Yet again, a relative element size $\overline{h} \leqslant 1$ is sufficient to capture the first three modes with acceptable accuracy.

4.5. Two-dimensional membrane model

Finally, a square isotropic membrane is studied with properties $L_x = L_y = 2$ m, $E = 70$ GPa, $\rho = 1$ kg/m^3, $T = 1$ N/m and $\ell = 0.2$ m, while all edges are modelled to be fixed. The relative errors of the natural frequencies corresponding to modes $(m = 1, n = 1)$, $(m = 1, n = 2)$, $(m = 2, n = 2)$ and $(m = 1, n = 3)$ of this membrane are shown in Fig. 10. As it can be observed, the results obtained by employing the higher-order II mass matrix (considering $\alpha = 3/4$) are those that present the lowest error, except in mode $(m = 1, n = 3)$, where those derived from the higher-order I mass matrix ($\alpha = 1/2$) do so. Note that for mode $(m = 1, n = 3)$, the convergence curve corresponding to the higher-order II mass matrix changes its slope considerably for $\overline{h} > 1$. Notice also that, apart from exhibiting much smaller errors, the higher-order II mass matrix leads to a solution that converges faster than those of the rest for modes $(m = 1, n = 1)$ and $(m = 2, n = 2)$, whereas in modes $(m = 1, n = 2)$ and $(m = 1, n = 3)$ it is similar. Finally, it is observed that, considering a relative element size $\overline{h} = 2$, the use of the higher-order II mass matrix leads to results within 1% accuracy, where for the higher-order I mass matrix this maximum error is 5%.

As an illustrative example, Fig. 11 shows the contour curves corresponding to the vibration shape of the considered membrane with fixed edges for the modes $(m = 1, n = 1)$ and $(m = 2, n = 2)$, employing the higher-order I mass matrix of the membrane model. It can be seen that taking a relative element size $\overline{h} \leqslant 1$ leads to a numerical model that accurately reproduces the behaviour given by the analytical solution, which is consistent with the observations for the rod and beam models.

5. Conclusions

In this work, several continuum models with micro-inertia have been discretized by means of finite elements, thereby separating the numerical length scale (i.e. the element size) from the physical length scale (i.e. the constitutive parameter accompanying the higher-order inertia terms). The main objective of this work has been to obtain suitable solutions of these continuum models through discrete matrix forms, considering element sizes larger than the corresponding length scale, with the aim of reducing the computational costs that would be needed to solve the equivalent discrete lattice system. To achieve this objective, the use of several mass matrices is proposed here for the first time in this kind of models. The numerical results are compared to corresponding analytical solutions. The vibration modes of micro-inertia extensions of the classical one-dimensional axial rod model, the beam bending theories of Euler–Bernoulli and Rayleigh, and the two-dimensional membrane model have been studied.

The overriding conclusion is that the use of higher-order mass matrices, which are a linear combination of the consistent mass matrix and either the lumped mass matrix (rods, membranes) or the stiffness matrix (beam theories) can significantly improve the accuracy of the numerical models – both in terms of absolute error and in terms of convergence rate (i.e. rate of error reduction upon refinement of the finite element mesh). A secondary conclusion is that the natural frequencies of the lower modes can be captured accurately with element sizes that are up to twice as large as the physical length scale – thus reducing the computational cost that would be necessary to solve an equivalent discrete lattice system accounting for scale effects. On the other hand, if the focus is on capturing the mode shape, rather than the natural frequency, more refined finite element meshes are required.

Data availability

No data was used for the research described in the article.

Declaration of Competing Interest

The authors declare that they have no known competing financial interests or personal relationships that could have appeared to influence the work reported in this paper.

Acknowledgements

The authors acknowledge support from MCIN/AEI/10.13039/501100011033 under Grants numbers PGC2018-098218-B-I00 and PRE2019-088002. FEDER: A way to make Europe. ESF invests in your future.

Appendix A. Boundary conditions for the beam problem

A simply supported beam is solved from Eq. (17) with boundary conditions $V(0) = 0, V_{xx}(0) = 0, V(L) = 0$ and $V_{xx}(L) = 0$, leading to

$$c_1 + c_3 = 0 \tag{A.1}$$

$$-c_1\psi^2 + c_3\phi^2 = 0 \tag{A.2}$$

$$c_1\cos(L\psi) + c_2\sin(L\psi) + c_3\cosh(L\phi) + c_4\sinh(L\phi) = 0 \tag{A.3}$$

$$\begin{aligned} &-c_1\left(\psi^2\cos(L\psi)\right) - c_2\left(\psi^2\sin(L\psi)\right) + c_3\left(\phi^2\cosh(L\phi)\right) \\ &+c_4\left(\phi^2\cosh(L\phi)\right) = 0 \end{aligned} \tag{A.4}$$

After solving these equations, the mode shape is found to take the format of

$$V_m(x) = C_m\sin\left(\frac{m\pi x}{L}\right) \tag{A.5}$$

with $m \in \mathbb{N}^+$.

Conversely, a cantilever beam is solved via boundary conditions $V(0) = 0, V_x(0) = 0, V_{xx}(L) = 0$ and $V_{xxx}(L) + \kappa V_x(L) = 0$. This yields

$$c_1 + c_3 = 0 \tag{A.6}$$

$$c_2\psi + c_4\phi = 0 \tag{A.7}$$

$$\begin{aligned} &-c_1\left(\psi^2\cos(L\psi)\right) - c_2\left(\psi^2\sin(L\psi)\right) + c_3\left(\phi^2\cosh(L\phi)\right) \\ &+c_4\left(\phi^2\sinh(L\phi)\right) = 0 \end{aligned} \tag{A.8}$$

$$\begin{aligned} &c_1\left(\psi^3\sin(L\psi) - \kappa\psi\sin(L\psi)\right) - c_2\left(\psi^3\cos(L\psi) - \kappa\psi\cos(L\psi)\right) \\ &+c_3\left(\phi^3\sinh(L\phi) + \kappa\phi\sinh(L\phi)\right) \\ &+c_4\left(\phi^3\cosh(L\phi) + \kappa\phi\cosh(L\psi)\right) = 0 \end{aligned} \tag{A.9}$$

which leads to a mode shape according to

$$\begin{aligned} &V_m(x) = C_m[(\cos(\psi_m x) - \cosh(\phi_m x)) \\ &-\tfrac{\psi_m^2\cos(\psi_m L)+\phi_m^2\cosh(\phi_m L)}{\psi_m^2\sin(\psi_m L)+\psi_m\phi_m\sinh(\phi_m L)}\left(\sin(\psi_m x) - \tfrac{\psi_m}{\phi_m}\sinh(\phi_m x)\right)] \end{aligned} \tag{A.10}$$

Table B.1
Natural frequencies and optimal value for α for the rod problem.

Number of elements	First eigenfrequency	Optimal α
2	$\omega = \frac{c_e}{\sqrt{\frac{3-\alpha}{24}\ L^2+\ell^2}}$	$\alpha = 0.5683$
3	$\omega = \frac{c_e}{\sqrt{\frac{6-\alpha}{54}\ L^2+\ell^2}}$	$\alpha = 0.5287$
4	$\omega = \frac{c_e}{\sqrt{\frac{6+3\sqrt{2}-\alpha}{96}\ L^2+\ell^2}}$	$\alpha = 0.5158$
5	$\omega = \frac{c_e}{\sqrt{\frac{9+3\sqrt{5}-\alpha}{150}\ L^2+\ell^2}}$	$\alpha = 0.5100$
6	$\omega = \frac{c_e}{\sqrt{\frac{12+6\sqrt{3}-\alpha}{216}\ L^2+\ell^2}}$	$\alpha = 0.5069$

Appendix B. Symbolic finite element results for the rod problem

For a limited number of finite elements, it is possible to solve the rod problem symbolically. This has been carried out for the fixed–fixed configuration for up to 6 equal-sized elements, and the lowest eigenfrequency was computed. The results are summarised in Table B.1 where $c_e = \sqrt{E/\rho}$. Next, an optimal value for the mass weighting constant α as defined in Eq. (33) has been computed by matching the numerical result, given as a function of α, to the analytical result of Eq. (4).

It is clear that the optimal value for α appears to converge to a value of $\alpha = \frac{1}{2}$. However, to verify the accuracy of this value a Richardson extrapolation of the numerically obtained values for α has been carried out based on

$$\alpha(h) \approx \tilde{\alpha} + A_1 h + A_2 h^2 + A_3 h^3 + A_4 h^4 \tag{B.1}$$

where $\alpha(h)$ is a numerical approximation of the unknown exact solution for α based on grid size h, while the various A_i are constants that are to be determined. In our case, the grid size h equals the bar length divided by the number of elements. This leads to a set of five simultaneous equations with unknowns A_1, A_2, A_3, A_4 and an *estimate* for the exact solution $\tilde{\alpha}$. Carrying out this extrapolation results in $\tilde{\alpha} \approx 0.5001$. This is in agreement with the earlier observation that $\alpha = \frac{1}{2}$ appears to be the optimal value.

References

[1] Rahmani A, Faroughi S, Sari M, Abdelkefi A. Selection of size dependency theory effects on the wave's dispersions of magneto-electro-thermo-elastic nano-beam resting on visco-elastic foundation. Eur J Mech-A/Solids 2022:104620.
[2] Yin YM, Li HY, Xu J, Zhang C, Liang F, Li X, et al. Facile fabrication of flexible pressure sensor with programmable lattice structure. ACS Appl Mater Interf 2021;13:10388–96.
[3] Caldas EM, Novatzky D, Deon M, de Menezes EW, Hertz PF, Costa TMH, et al. Pore size effect in the amount of immobilized enzyme for manufacturing carbon ceramic biosensor. Microporous Mesoporous Mater 2017;247:95–102.
[4] Wisnom M. Size effects in the testing of fibre-composite materials. Compos Sci Technol 1999;59:1937–57.
[5] Civalek Ö, Dastjerdi S, Akbaş ŞD, Akgöz B. Vibration analysis of carbon nanotube-reinforced composite microbeams. Mathe Methods Appl Sci 2021:1–17.
[6] Lee D, Nguyen DM, Rho J. Acoustic wave science realized by metamaterials. Nano Convergence 2017;4:3.
[7] Zaera R, Vila J, Fernández-Sáez J, Ruzzene M. Propagation of solitons in a two-dimensional nonlinear square lattice. Int J Non-Linear Mech 2018;106:188–204.
[8] Andresen S, Bäger A, Hamm C. Eigenfrequency maximisation by using irregular lattice structures. J Sound Vib 2020;465:115027.
[9] Syam WP, Jianwei W, Zhao B, Maskery I, Elmadih W, Leach R. Design and analysis of strut-based lattice structures for vibration isolation. Precision Eng 2018;52:494–506.
[10] Erofeyev VI. Wave processes in solids with microstructure, vol. 8. World Scientific; 2003.
[11] Jakata K, Every A. Determination of the dispersive elastic constants of the cubic crystals Ge, Si, GaAs, and InSb. Phys Rev B 2008;77:174301.
[12] Philippidis T, Aggelis D. Experimental study of wave dispersion and attenuation in concrete. Ultrasonics 2005;43:584–95.
[13] Aggelis D, Polyzos D, Philippidis T. Wave dispersion and attenuation in fresh mortar: theoretical predictions vs. experimental results. J Mech Phys Solids 2005;53:857–83.
[14] Mindlin RD. Microstructure in linear elasticity, Tech. Rep., Columbia Univ., New York, Dept. of Civil Engineering and Engineering Mechanics; 1963.
[15] Eringen AC. Linear theory of micropolar elasticity. J Mathe Mech 1966;15:909–23.
[16] Eringen AC, Edelen D. On nonlocal elasticity. Int J Eng Sci 1972;10:233–48.
[17] Krumhansl JA. Generalized continuum field representations for lattice vibrations. Lattice dynamics. Elsevier; 1965. p. 627–34.
[18] Krumhansl J. Some considerations of the relation between solid state physics and generalized continuum mechanics. In: Mechanics of generalized continua. Springer; 1968. p. 298–311.
[19] Zhang B, Li H, Kong L, Shen H, Zhang X. Coupling effects of surface energy, strain gradient, and inertia gradient on the vibration behavior of small-scale beams. Int J Mech Sci 2020;184:1–21.
[20] Abdelrahman AA, Esen I, Özarpa C, Eltaher MA. Dynamics of perforated nanobeams subject to moving mass using the nonlocal strain gradient theory. Appl Math Model 2021;96:215–35.
[21] Harbola V, Crossley S, Hong SS, Lu D, Birkholzer YA, Hikita Y, et al. Strain gradient elasticity in $SrTiO_3$ membranes: bending versus stretching. Nano Lett 2021;21:2470–5.
[22] Liu C, Yu J, Xu W, Zhang X, Wang X. Dispersion characteristics of guided waves in functionally graded anisotropic micro/nano-plates based on the modified couple stress theory. Thin-Walled Struct 2021;161:1–11.
[23] Polyzos D, Fotiadis D. Derivation of Mindlin's first and second strain gradient elastic theory via simple lattice and continuum models. Int J Solids Struct 2012;49:470–80.
[24] Bacigalupo A, Gambarotta L. Generalized micropolar continualization of 1D beam lattices. Int J Mech Sci 2019;155:554–70.
[25] Gómez-Silva F, Fernández-Sáez J, Zaera R. Nonstandard continualization of 1D lattice with next-nearest interactions. Low order ODEs and enhanced prediction of the dispersive behavior. Mech Adv Mater Struct 2020:1–10.
[26] Gómez-Silva F, Zaera R. Novel Enriched Kinetic Energy continuum model for the enhanced prediction of a 1D lattice with next-nearest interactions. Compos Struct 2022;281:115003.
[27] Challamel N, Zhang Z, Wang C, Reddy J, Wang Q, Michelitsch T, et al. On nonconservativeness of Eringen's nonlocal elasticity in beam mechanics: correction from a discrete-based approach. Arch Appl Mech 2014;84:1275–92.
[28] Gómez-Silva F, Zaera R. Analysis of low order non-standard continualization methods for enhanced prediction of the dispersive behaviour of a beam lattice. Int J Mech Sci 2021;196:1–11.
[29] Gómez-Silva F, Zaera R. Low order nonstandard continualization of a beam lattice with next-nearest interactions: Enhanced prediction of the dynamic behavior. Mech Adv Mater Struct 2021:1–15.
[30] Zhang Z, Challamel N, Wang C. Eringen's small length scale coefficient for buckling of nonlocal Timoshenko beam based on microstructured beam model. J Appl Phys 2013;114:114902.
[31] Duan WH, Challamel N, Wang C, Ding Z. Development of analytical vibration solutions for microstructured beam model to calibrate length scale coefficient in nonlocal Timoshenko beams. J Appl Phys 2013;114:104312.
[32] Gómez-Silva F, Zaera R. Dynamic analysis and non-standard continualization of a Timoshenko beam lattice. Int J Mech Sci 2022;214:106873.
[33] Gómez-Silva F, Zaera R. New low-order continuum models for the dynamics of a Timoshenko beam lattice with next-nearest interactions. Comput Struct 2022;272:106864.
[34] Andrianov I, Awrejcewicz J. Continuous models for 2D discrete media valid for higher-frequency domain. Comput Struct 2008;86:140–4.
[35] Lombardo M, Askes H. Elastic wave dispersion in microstructured membranes. Proc Roy Soc A: Mathe Phys Eng Sci 2010;466:1789–807.
[36] Gómez-Silva F, Zaera R. Low-order non-classical continuum models for the improved prediction of an anisotropic membrane lattice's dynamics. Thin-Walled Struct 2022;179:109632.
[37] Gómez-Silva F, Zaera R. Low-order continualization of an anisotropic membrane lattice with next-nearest interactions. Enhanced prediction of its dynamic behaviour. Eur J Mech- A/Solids 2023;97:104801.
[38] Challamel N, Hache F, Elishakoff I, Wang C. Buckling and vibrations of microstructured rectangular plates considering phenomenological and lattice-based nonlocal continuum models. Compos Struct 2016;149:145–56.
[39] Hache F, Challamel N, Elishakoff I, Wang C. Comparison of nonlocal continualization schemes for lattice beams and plates. Arch Appl Mech 2017;87:1105–38.
[40] Papargyri-Beskou S, Polyzos D, Beskos D. Wave dispersion in gradient elastic solids and structures: a unified treatment. Int J Solids Struct 2009;46:3751–9.
[41] Froiio F, Zervos A, Vardoulakis I. On Natural Boundary Conditions in Linear 2nd-Grade Elasticity; 2010.
[42] Froiio F, Zervos A. Second-grade elasticity revisited. Mathe Mech Solids 2019;24:748–77.
[43] Askes H, Wang B, Bennett T. Element size and time step selection procedures for the numerical analysis of elasticity with higher-order inertia. J Sound Vib 2008;314:650–6.
[44] Wang Z-P, Sun C. Modeling micro-inertia in heterogeneous materials under dynamic loading. Wave Motion 2002;36:473–85.
[45] Metrikine AV, Askes H. One-dimensional dynamically consistent gradient elasticity models derived from a discrete microstructure: Part 1: Generic formulation. Eur J Mech-A/Solids 2002;21:555–72.
[46] Andrianov I, Awrejcewicz J. Continuous models for 1D discrete media valid for higher-frequency domain. Phys Lett A 2005;345:55–62.

[47] Engelbrecht J, Berezovski A, Pastrone F, Braun M. Waves in microstructured materials and dispersion. Phil Mag 2005;85:4127–41.
[48] Metrikine A, Askes H. An isotropic dynamically consistent gradient elasticity model derived from a 2D lattice. Phil Mag 2006;86:3259–86.
[49] Madeo A, Neff P, Aifantis EC, Barbagallo G, d'Agostino MV. On the role of micro-inertia in enriched continuum mechanics. Proc Roy Soc A: Mathe Phys Eng Sci 2017;473:20160722.
[50] Ayad M, Karathanasopoulos N, Ganghoffer J-F, Lakiss H. Higher-gradient and micro-inertia contributions on the mechanical response of composite beam structures. Int J Eng Sci 2020;154:103318.
[51] De Domenico D, Askes H. Stress gradient, strain gradient and inertia gradient beam theories for the simulation of flexural wave dispersion in carbon nanotubes. Compos Part B: Eng 2018;153:285–94.
[52] Askes H, Nguyen DC, Tyas A. Increasing the critical time step: micro-inertia, inertia penalties and mass scaling. Comput Mech 2011;47:657–67.
[53] Han SM, Benaroya H, Wei T. Dynamics of transversely vibrating beams using four engineering theories. J Sound Vib 1999;225:935–88.
[54] Lombardo M, Askes H. Lumped mass finite element implementation of continuum theories with micro-inertia. Int J Numer Meth Eng 2013;96:448–66.
[55] Tkachuk A, Bischoff M. Direct and sparse construction of consistent inverse mass matrices: general variational formulation and application to selective mass scaling. Int J Numer Meth Eng 2013;101:435–69.
[56] Hughes TJ. The finite element method: linear static and dynamic finite element analysis. Courier Corporation; 2012.
[57] Zuo Z, Li S, Zhai C, Xie L. Optimal lumped mass matrices by minimization of modal errors for beam elements. J Vib Acoust 2014;136.
[58] Kim K-O. A review of mass matrices for eigenproblems. Comput Struct 1993;46:1041–8.